Nuclear Engineering and Design 429 (2024) 113612

Contents lists available at ScienceDirect

Nuclear Engineering and Design

journal homepage: www.elsevier.com/locate/nucengdes

High-Throughput falling ball viscometer for measuring High-Temperature molten salts

Alexander Levy [a,*], Yifan Zhang [b], Haoxuan Yan [c], Anubhav Wadehra [c], Yu Zhong [b], Karl Ludwig [c,d], Uday Pal [a,c]

[a] Department of Mechanical Engineering, Boston University, 110 Cummington Mall., Boston Massachusetts, 02215, USA
[b] Department of Mechanical and Materials Engineering, Worster Polytechnic Institute, 100 Institute Rd., Worcester, MA, 01609, USA
[c] Division of Materials Science and Engineering, Boston University, 15 St. Marry's St., Boston MA 02215, USA
[d] Department of Physics, Boston University, 590 Commonwealth Ave., Boston Massachusetts, 02215, USA

A B S T R A C T

The demand for clean energy production and storage has increased interest in molten salt technologies, including Molten Salt Reactors (MSR). Understanding of how molten salts properties change with respect to temperature and structure is vital to establishing efficient, cost effective MSR systems. Research into these materials however has been limited due to the difficulty in accurately measuring properties of these reactive materials at elevated temperatures and controlled environment in a time efficient way. Much research has turned to molecular dynamic (MD) modeling to alleviate these issues. This research presents a custom fabricated falling ball viscometer system for measuring molten salt viscosity quickly. A model for correlating velocity to viscosity for $Re < 300$ was also developed for use with this system. The viscometer is demonstrated on eutectic FLiNaK and NaF-ZrF4 (53–47 mol%) up to 150 K above the respective melting points. The results are compared to MD simulations to verify their effectiveness for predicting viscosity and previously reported measurements.

1. Introduction

There is a resurgence of interest in molten salts in energy sector technologies (Liu et al., 2022; Mao et al., 2022; Bhatnagar et al., 2022) including Molten Salt Reactors (G.E.N.-IV International-Forum, 2009; Holcomb and Cetiner, 2010) bringing a need for rapid material research on these systems. Thermophysical properties such as density, surface tension, heat capacity and thermal conductivity are key areas of study for these materials, both experimentally and theoretically. Viscosity is one thermophysical property that is highly correlated with molten salt speciation and structure, and influences the salt lifecycle and recycling, and general mechanical design of the reactor system (Workshop, 2017).

Two common methods for measuring the viscosity of these molten salts employ the rotational rheometer (Tkacheva et al., 2022; Rose et al., 2022) and the oscillatory damped viscometer (Korklep and Oye, 1979; Ito et al., 1989). While both methods have been proven to be reliable, they pose inherent issues for use with molten salts. Rotational rheometers typically follow the cheaper method of purchasing a commercial instrument and modifying it with a furnace to accommodate the high temperature needs or purchasing the more expensive system with the furnace together (Bhattad, 2023). These systems require multiple load measurements to be taken at different angular velocities of a rotating spindle in a steady state condition. Due to the number of individual data points, these measurements can take more time at a given set temperature and have varying levels of accuracy based on operating parameters.

An oscillatory damped viscometer measures the damping effect of the molten salt on an oscillating cup at a known rotational frequency. Since these systems still require appropriate steady state behavior, multiple test frequencies are not necessarily required like rotational viscometers. However, rotational variance due to friction and environmental damping can lead to error due to other effects if not appropriately accounted for, especially when factoring thermal effects of temperature.

Both methods require vessel, spindle, and containment to be carefully considered for use with the molten salts. These customizations and commercial high temperature versions can considerably increase the cost and complexity of these systems.

More recently there is additional work on a rolling ball viscometer with a controllable incline to control the rate, and therefore Reynolds Number (Re). This method shows initial promise since it allows for high control over a range of Reynolds conditions, in this case using a calibration method to relate specific Re conditions to viscosity over a range of Re above the Stokes flow or creeping flow regime ($Re > 1$). System

* Corresponding author.
E-mail address: levyalex@bu.edu (A. Levy).

https://doi.org/10.1016/j.nucengdes.2024.113612
Received 25 June 2024; Received in revised form 24 August 2024; Accepted 22 September 2024
Available online 10 October 2024

material and sensing mechanisms can also be easily changed based on salt requirements. (Birri et al., 2023).

Like the rolling ball viscometer, the classic falling ball viscometer is one alternative that has not yet been fully explored in depth for measuring molten salts. This method typically depends on Stokes Law for the estimation of drag force on the ball. For fluid samples bound in a tube with a circular cross section, like most examples for this method, the Faxen Correction Equation is utilized to account for the effect of a circular vessel wall on the fluid flow, often called the wall effect (Brizard et al., 2005). While this method has been shown to be highly accurate under Stokes Flow conditions, the low Re regime highly limits the effective use of this method. To maintain low Reynold's numbers, the fluid either needs to have a high viscosity, or have a minimized difference between the sphere (ρ_s) and fluid (ρ_f) densities. Unlike other methods, falling ball viscometers do not require various testing states, and most of the effect of temperature can easily be accounted for by simple thermal expansion changes. They are also easily adaptable to a wide range of materials and measurement methods (Sobczak, 1986; Powell et al., 1989).

Additionally, there is significant research in flow around a sphere at a wide range of Re numbers. Because of this there have been many attempts at designing formulas and methods to apply this concept to higher Re ranges, including calibrating the systems to unbound Reynolds number (Re_∞) behavior, or creating fitted trends to experimental data (Bougas and Stamatoudis, 1993; Singh et al., 2012). Because of the wide span of flow behaviors observed over varying Re ranges, including flow separation, attached and unattached eddy currents and flow oscillations (Johnson and Patel, 1999), most empirical models don't reflect all regions of flow accurately or are represented by a complex relationship between viscosity and velocity. Additionally careful design considerations must be made to ensure these flow regimes do not become dominated by inertial or velocity dependent drag as flow becomes more complex.

This work presents a low-cost, high-throughput falling ball viscometer method adapted to take high-temperature viscosity measurements that minimizes sample size, shortens measurement time compared to existing measurements at each temperature (focusing on actual measurement time, not temperature settling time) and is easily adaptable to various material requirements. This method expands on the classic falling ball viscometer method, using experimentally validated computational fluid dynamic methods (CFD) (Wahl et al., 2021; Feng et al., 2006) to represent the relationship between velocity and viscosity for a higher range of $Re_{ball}(< 315)$ with a custom-made solenoid coil sensor for velocity measurements. Two fluoride salt candidates for Molten Salt Reactors (MSR) were tested as a proof of concept. The first is a well-studied general fluoride salt, eutectic LiF-NaF-KF (46.5–11.5–42 mol %, FLiNaK), used as a general application fluid including primary and secondary coolant applications (Williams et al., 2006). The second is the lesser studied NaF-ZrF_4 (53–47 mol%) representing the fuel salt carrier candidate NaF-ZrF_4-UF_4 (53–41-6 mol%) used in the Aircraft Reactor Experiments from the 1950 s (Workshop, 2017; Cottrell et al., 1955; Serrano-Lopez and Cuesta-Lopez, 2013) with different variations still considered today. The accuracy of this method is demonstrated by comparing experimental results to simulated viscosities from MD modeling and results from previously reported studies.

2. Materials and methods

The falling ball viscometer is designed for use in a small form factor inert glove box environment. A customized furnace was developed to support the required temperature stability and viscometer geometry needed. Additionally, this furnace was designed around the need for sample preparation and to accommodate additional future property measurements. Functionality of the furnace additionally must not interfere with the operation of a small form factor glove box. The viscometer, as shown in Fig. 1, consists of a ball drop mechanism to quickly load and drop the 3 mm Ti spheres (balls) into the molten salt near the fluid surface. Two solenoid coils with calibrated spacing are used to detect the presence of metallic sphere (Kobbekaduwa and Wijayaratnam, 2012) by measuring the change in voltage through the coils using a detection circuit driven by an Arduino Uno microcontroller. The voltage signals are then post processed and a velocity is determined. Using the fluid flow model representing the physical relationship, the measured terminal velocity is used to derive the corresponding viscosity at each temperature. Each component is described further in the following sections.

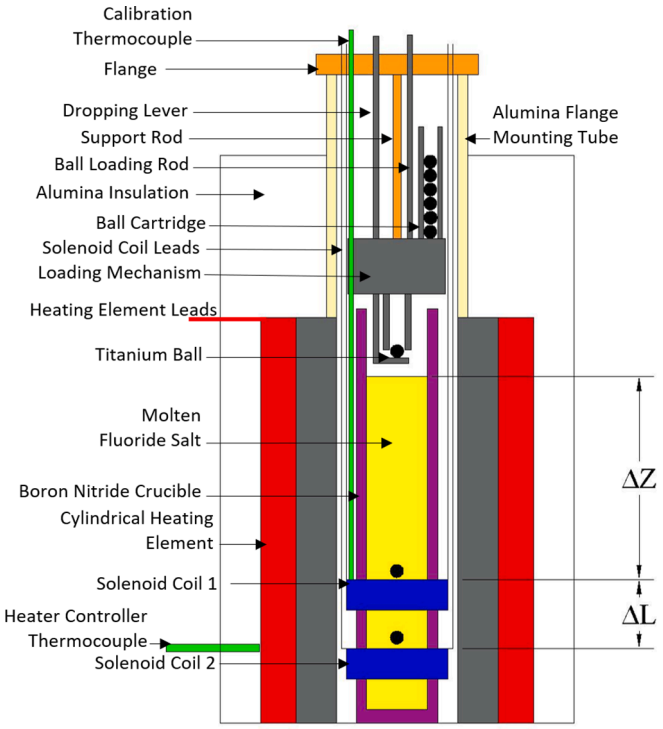

Fig. 1. Diagram of high temperature falling ball viscometer design (not to scale) illustrating the basic setup of the vertical cylindrical heater, thermal conductor with cavity for the sample and solenoid sensors as positioned inside the glove-box sized furnace.

2.1. Material synthesis and characterization

Materials are synthesized with procedures that mostly follow those used by Argonne National Lab (Rose et al., 2022). Samples for both NaF-ZrF_4 (53–47 mol%) and FLiNaK (46.5–11.5–42 mol%) were prepared in an Argon filled glove box with 1 ppm or lower of O_2 and H_2O. Precursors are obtained as single component powders from Sigma Aldrich. Each precursor is baked on a hot plate at 553 K (280 °C) for 2 h in a Ni-200 crucible that was polished with high grit sandpaper and then cleaned thoroughly to remove oxides using alcohol (Alpha Aser PN: 22930-M6). After baking, the reagent salts are weighed and mixed. The mixture is added to a similarly polished and cleaned Ni-200 crucible and melted in a furnace in the glove box, first additionally baking the sample at 553 K for 1 h then raising the temperature to 100 K above the respective melting point for 2 h. Samples are crushed to powder using a nickel mortar and pestle to help guarantee uniformity for next steps. Specification sheets for precursors and the alcohol used are provided as supplementary information. The crushed salt mixture is then added to fill a Boron Nitride (BN99 or HCBN) crucible that is 150 mm tall with 9 mm ID and 14 mm OD. Enough salt is added so that the maximum molten salt height is between 101 mm (4″) and 108 mm (4.25″). The salt is then melted inside the glovebox at approximately 100 K above the respective melting point and held for 2 h before returning the BN crucible to room

temperature.

Representative samples of as prepared and post measurement salts were analyzed for impurities and composition with XRD, examples shown in Figs. 2 and 3. Only $NaFZrF_4$ was analyzed with SEM/EDS and not FLiNaK because it is found to be too hygroscopic. Some representative samples were also analyzed by DSC/TGA and ICP-OES methods to guarantee procedural accuracy. At each melting step mass is measured to verify no mass loss occurs due to reactions or volatility. Additionally, samples are visually inspected for any discoloration or obvious particulate in the samples that could indicate impurity interactions.

2.2. Velocity viscosity relationship: Modeling

The typical viscosity (η) – velocity (U) relationship that utilizes Stokes Law to represent drag force in the Creeping Flow Regime or Stokes Flow is used to inform the numerical model. For a sphere of radius (r_s), a force balance relationship (1) is used, showing drag force F_D (2), buoyancy force F_B (3) of a fluid with density ρ_f, and gravitational acceleration F_g (4) of the sphere with density ρ_s. For flow with Reynold's Number (5) beyond Stokes Flow an additional factor for the drag force due to flow separation and increasing turbulence k is often applied. (Happel et al., 1993)

$$F_D - F_B = F_g \tag{1}$$

$$F_D = 6\pi\eta r_s U k \tag{2}$$

$$F_B = \frac{4}{3}\pi r_{bs}^3 \rho_f g_z \tag{3}$$

$$F_g = \frac{4}{3}\pi r_s^3 \rho_s g_z \tag{4}$$

$$Re = \frac{2\rho_f U r_s}{\eta} \tag{5}$$

An accurate representation of the k factor requires a reasonable solution of the Navier-Stokes equations (6) across a range of different flow behavior that presents as Re increases. (Happel et al., 1993)

$$\rho_f\left(\frac{\partial \vec{v}}{\partial t}\right) + \rho_f(\partial \vec{v} \bullet \nabla \vec{v}) = -\nabla P + \rho_f \vec{g} + \mu \nabla^2 \vec{v} \tag{6}$$

To eliminate the need for experimental determination for k, a numerical model with the appropriate considerations is utilized. In COMSOL, using the Laminar Flow fluid module, the force components from Stokes Law are applied to represent the appropriate flow. With a fixed reference frame at the center of the sphere, a no slip condition is applied to the surface of the sphere. A translating wall with a no slip condition is applied to the crucible surface. The inlet of flow is assigned to the bottom of the crucible with the outlet at the top, indicating flow in a positive axial direction. Global weak constraints are applied to establish the correct relationship between displacement (7), velocity (8) and acceleration (g). (COMSOL, 2024)

$$\boldsymbol{X}(t) = \boldsymbol{X}(t-1) - t\dot{\boldsymbol{X}}(\boldsymbol{t}) \tag{7}$$

$$\dot{\boldsymbol{X}}(t) = \ddot{X}(t) - \left(\frac{F_D}{V_s\rho_s} - \frac{F_B}{V_s\rho_s}\right)t \tag{8}$$

Fluid temperature is represented by density at the given temperature, $\rho_f(T)$. Geometric parameters are defined to reflect nominal or as measured values of the physical system with thermal expansion corrections for the sphere and crucible respectively (9).

$$r_{eff} = r_{nom} + r_{nom}\alpha\Delta T \tag{9}$$

The resultant drags (10) and local velocity is then determined through COMSOL's solver. Based on the calculated results, the maximum possible velocity of the ball is determined to be the velocity of the flow at the inlet.

$$F_{drag} = \iint_{S_{sphere}} \tau_{w_z}\, dS_{sphere} \tag{10}$$

Where shear force is determined in COMSOL by first determining the friction velocity matrix along the surface (u_τ) (11) based on the local shear at the wall, then finding the direction component of the shear (τ_{w_z}) (12). (Lyu, 2015)

$$u_\tau = \sqrt{\frac{\tau_w}{\rho}} \tag{11}$$

$$\tau_{w_z} = \rho u_\tau^2 \frac{u_z^T}{u^T} \tag{12}$$

Using this model, a "lookup table" is generated by solving for a velocity over a range of viscosities at a given fluid density. For each temperature, a correlation between viscosity and velocity can be determined by fitting a logarithmic regression to the data, represented by Equation (13), where g and h are the coefficients. Determined coefficients correlating for each temperature for the salts measured in this work are included as supplementary information in Tables S-4 and S-5. To check the accuracy, the model can be re-run using this derived viscosity, and the resultant terminal velocity can be compared to the measured velocity.

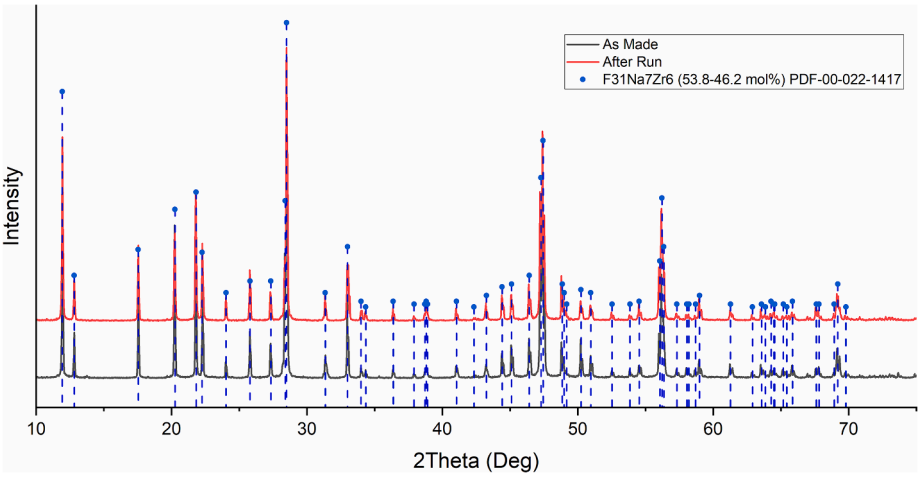

Fig. 2. XRD of NaF-ZrF_4 (53–47 mol%) of as made salt sample compared to after run sample, with $Na_7Zr_6F_{31}$ PDF used as a baseline for comparison.

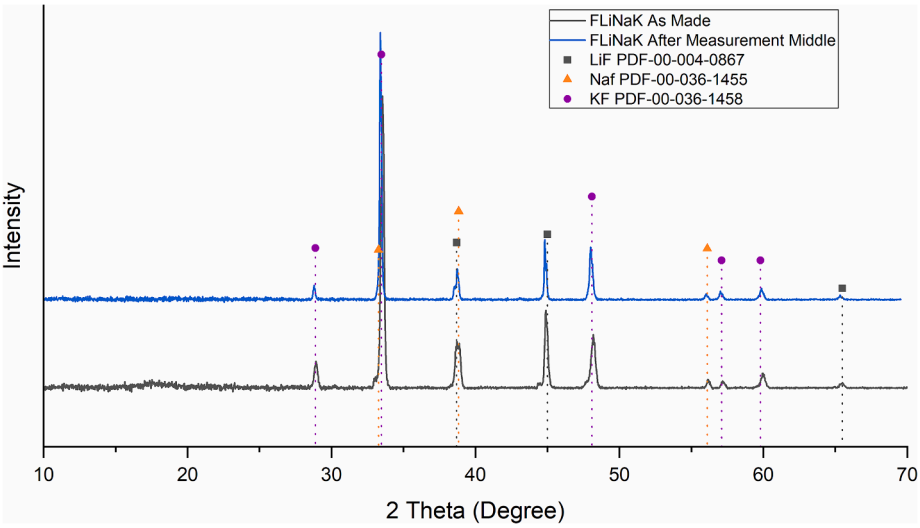

Fig. 3. XRD of FLiNaK of as made salt sample compared to after run sample with appropriate precursor PDF comparison.

$$v_{measured} = m^{*}\ln(\mu) + b \tag{13}$$

Validation of this model was performed using water (1 cPs) and Brookfield silicon oil standards with viscosities of 4.8 cPs, 9.4 cPs and 96 cPs using a room temperature version of the viscometer. Different ball materials including Aluminum (Alloy 2017) and Titanium (Alloy Gr-5) with a 3.175 mm (1/8″) diameter and acrylic tube diameters (5 mm and 9 mm) were used to reach a range of Re regimes to represent the expected range during the high-temperature experiments. It was found that the overall average remained accurate to the standards with good agreement between the COMSOL model and room temperature experiments for Re up to 250 (limitation set by room temperature properties of available materials), as shown in Fig. 4. Average velocities and standard deviations of experimental data for each flow condition are provided are as supplementary information in Tables S-6. Some high-temperature experiments may exceed this Re range slightly (Re ≈ 320) but since the flow regime is similar, the error is expected to be acceptable from the model in those ranges; the regimes correlate with the start of turbulent flow from other studies focusing on flow regimes around a sphere (Johnson and Patel, 1999; Happel et al., 1993). Higher Re regimes measured using water indicate the possibility of inaccuracies in the model due to the laminar flow assumption, or indicate terminal velocity was not reached during these measurements.

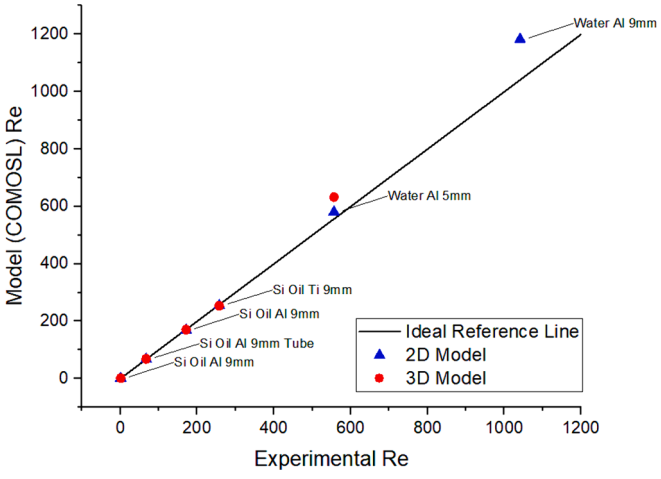

Fig. 4. COMSOL derived velocities of Brookfield Standards compared to room temperature experimental results.

2.3. Sensors: High temperature solenoid coils

The sensor component consists of two solenoid coils made from 30-gauge Ni-200 wire. Other easy to form wire materials including copper or stainless steel were shown to have higher levels of corrosion or significant loss of yield strength resulting in lead breakage.

To fabricate the coils, steps depicted in Fig. 5 are employed. The wire is wrapped around a 14 mm blank, the same diameter as the crucible. This way the coils are tight against the crucible, maximizing signal sensitivity. The coils are each made with approximately 12.4 mm (1/2″) long leaving a gap approximately the size of the wire gauge between each turn to prevent shorting, resulting in about 18 to 20 turns for each coil. To hold the coil shape, the wire is encapsulated with ceramic paste (AREMCO Ceramabond 552-VFG). After drying of the ceramic paste, two individual coils are attached with the same paste where the space between the coils is 2 to 5 mm apart. A 12 mm alumina spacer is added to the bottom so the assembly can rest on the bottom of the furnace, resulting in a total coil height of approximately 40 mm. Excess wire is left unwrapped to act as leads for each coil and fed through 1/8″ double bore alumina tubes. The alumina tubes are pasted in place, parallel to the axis of the coil. The whole assembly is then fired in an Ar atmosphere following the curing procedure of the paste.

The finished two solenoid assembly is then calibrated at room temperature using the Brookfield viscosity standards used to validate the COMSOL model and a linear actuator driven by a stepper motor with a set velocity. The spacing between the coils (ΔH) is calculated from the set or expected velocity. (14) The same principle is applied for determining velocity from the measurements using the calibrated ΔH.

$$\Delta H = v_{expected}\Delta t \tag{14}$$

When the ball is at the center of one of these coils, the signal observed using the detection circuit is observed to be the minimum point. The circuit and signal analysis for determination of the minimum point are described in Section 2.4. Average coil spacing data and respective standard deviations are provided as supplementary information in Tables S-7 and S-8.

2.4. Ball detection

To determine the time for the ball to fall between coils centers, each coil attached to an LC circuit, modified with a diode between the inductor and capacitor, as shown in Fig. 6. Both circuits are controlled with an Arduino Uno as a micro-controller and excited with several

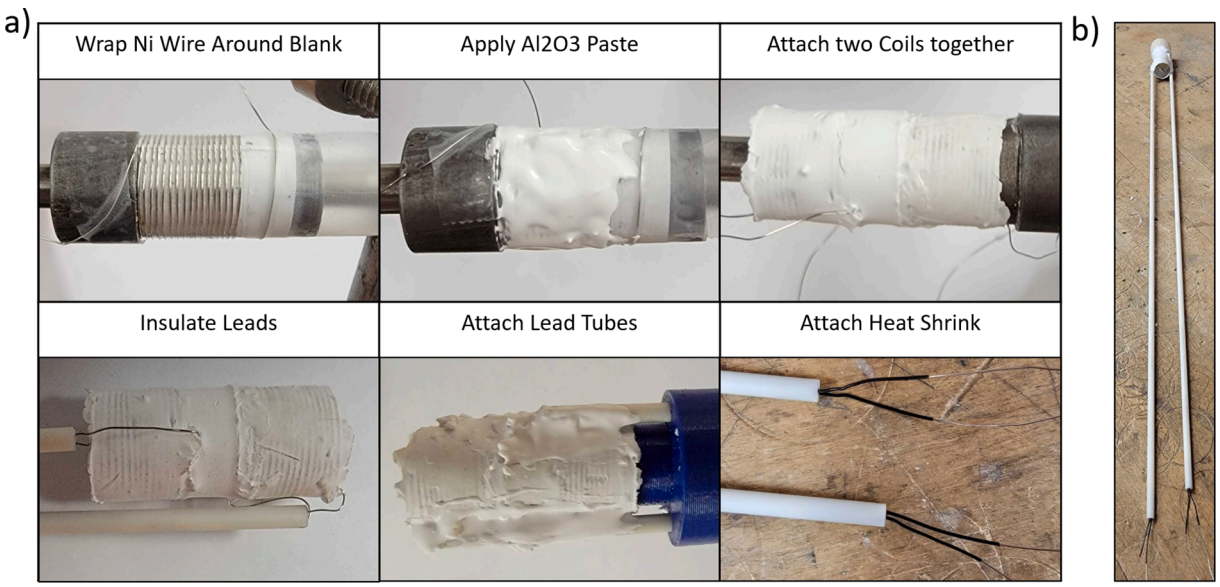

Fig. 5. Assembly of (a) solenoid coils from start to finish, excluding the curing steps and attachment of the bottom spacer and (b) the finished assembly.

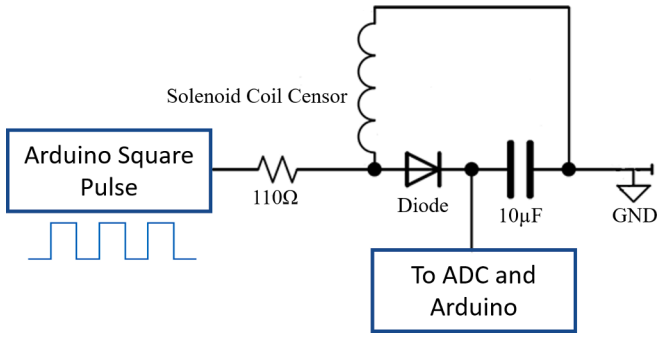

Fig. 6. Circuit loop of modified tank circuit for proximity detection of metallic balls.

square wave pulses for each measurement interval.

When the ball falls through the coil, a change of inductance ΔL is caused due to sphere material's volume percent in the magnetic field of the coil with N turns, cross sectional area A and axial length (h). It causes a change in the coil's average relative permeability $\Delta\overline{\mu_r}$ (15) and a change in the resonance frequency Δf (16) based on the capacitance (C).

$$\Delta L \propto \frac{\mu_o \Delta\overline{\mu_r} NA}{h} \tag{15}$$

$$\Delta f \propto \frac{1}{2\pi\sqrt{\Delta LC}} \tag{16}$$

This is observed as a change voltage ΔV due to a change of impedance ΔX_L (17) (18) with constant current (I). Additionally, frequency may also change based on the change of inductance.

$$\Delta V_L = I\Delta X_L \tag{17}$$

$$\Delta X_L = 2\pi\Delta f\Delta L \tag{18}$$

The change of impedance reduces the charge (Q) of the capacitor of capacitance C, indicating the presence of the sphere in the coil. Since the circuit is driven by frequency-based signal from the Arduino, the capacitor charge is built up after several pulses. The charge of the capacitor then amplifies the change in voltage from the inductor due to the dependance of voltage drop (ΔV_c) based on capacitor charge (19). Response time and sensitivity are optimized based on the capacitor size.

$$Q = C\Delta V_c \tag{19}$$

The voltage over the capacitor is measured by passing the signal through a 16-bit ADC (PN: TLC4541) and recorded by the microcontroller. The time dependent series of data averages is then sent and saved to the PC for additional signal processing; the averages are saved to minimize data transfer through serial communication.

A post processing code is then used to find the relative minimum voltage, or the point when the ball is assumed to be at the center of the coil with respect to the z axis. Here, a low pass filter is implemented to remove much of the noise. (Filtered signal example, Figure S-4) The low pass cutoff frequency is determined to be slightly higher than the expected terminal velocity (v) and 2 times the length of one coil (the sphere's position with respect to time represents ½ a period in the signal), nominally 12.4 mm (1/2″) (20).

$$f_{cutoff} = \frac{v}{2L_{coil}} \tag{20}$$

The expected velocity is determined with the COMSOL model and properties from previously reported studies, but the measured velocity must also agree with the cutoff frequency. The standard deviation is expected to be minimized at the point where frequency and velocity agree for a set of data points at a given temperature, showing agreement between measurements. A graphical example of this is provided as supplementary information as Figure S-5).

2.5. Drop mechanism

The drop mechanism, shown in Fig. 7, is made from a combination of 304 and 400 series stainless steel that allows multiple balls to be loaded prior to loading the assembly into the furnace. A carousel mechanism is rotated 180 degrees to load an individual ball from the loading tube to the dropping tube, which has the lower end positioned directly over the molten salt inside the BN crucible. A lever is then actuated to drop the ball from the dropping tube (opened condition). When complete, the lever can be reset (closed condition), and another ball loaded without opening the furnace. This helps to maintaining temperature stability, minimizing impurities in the salt and optimizes the data collection rate.

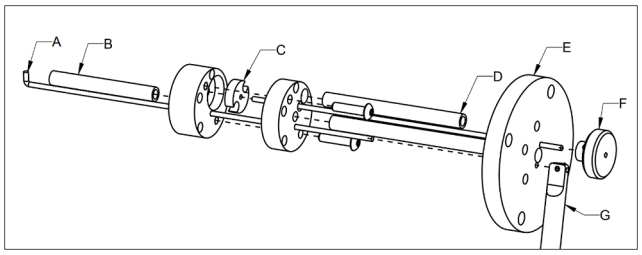

Fig. 7. Ball Drop assembly exploded view A) Dropping rod B) Load ball in this tube before dropping C) Loading Mechanism D) Tube for balls waiting to be loaded E) Mounting Flange F) Knob for loading balls G) lever for turning dropping rod.

2.6. Molten salt measurements

The ball drop mechanism and sensor, assembled as shown in Fig. 8.a, are placed inside the glove box where the Boron Nitride sample filled crucible is inserted into the solenoid assembly. The assembly is inserted into an alumina tube with a compact flange body attached to the top using compressed O-rings to hold it in place (Fig. 8.b.). The flange top is screwed to the flange body. The assembly is then inserted into the furnace opening. The bottom of the alumina tube then rests on top of the thermal conductor shown in Fig. 1. Temperature is then increased to the desired measurement temperature at 2 K/min. The desired set temperature is held for 30 min to stabilize prior to starting measurements. An additional thermocouple is inserted adjacent to the outer surface of the crucible just above the solenoid coils. Temperature of this thermocouple is observed during this stabilization period for changes. If no significant changes are observed, measurements are started. Additionally, this temperature is digitally recorded as the fluid temperature. For each temperature, 2 to 3 spheres are dropped into the salt, restarting the data gathering program in between. It takes approximately 1 to 2 min to load and drop the ball. After completing measurements at each temperature, the temperature is raised or lowered to the next set point. Ball dropping is stopped when space beneath the bottom coil fills up, and the balls start to collect in the region detectable by the bottom coil. This is observed as the bottom coil signal starts to represent a step function or the signal not returning to the same baseline after the ball is detected by the coil.

The minimum measurement temperature was 30 K above the expected melting point. The maximum measurable temperature was determined by analyzing the variation of ball velocity in the salt as a function of temperature. If terminal velocity is not being reached, the velocity begins to decrease with an increase in temperature. The point where this begins to happen is determined to be the maximum possible temperature due to an inadequate distance available in the column to attain terminal velocity because of limited drag from lower density and viscosity. This behavior can be seen as part of supplementary information in Figure S-6. Additionally, the distance to reach terminal velocity is determined based on the volume of salt available for the ball to accelerate. At the maximum temperature, the salt height (101–108 mm) minus the height of the coils (40 mm) gives approximately 60 mm distance for the ball to accelerate. This temperature for when terminal velocity is not reached coincides with the predicted distance from the laminar flow model (Figure S-8). A shorter distance associated with maximum temperature (50 mm) is selected to add a factor of safety to ensure terminal velocity is reached.

2.7. MD methods

Simulated viscosity values were determined using MD methods for both salts. Using the Matlantis platform, a universal neural network potentials (NNP) called Preferred potentials (PFP) (Takamoto et al., 2022) is used to evaluate the interatomic forces between ions in supercell. MD simulations are performed for eutectic FLiNaK and NaF-ZrF_4 53–47 mol% ranging from 798 K to 1123 K.

The initial configurations are generated from Packmol (Martinez, 2009) with random structure and avoiding atomic overlap, which contains a total of 432 and 1056 atoms for FLiNaK and NaF-ZrF_4, respectively. The equilibrium volumes at different temperatures are selected from the existing literature (Janz (1988), Cohen (1956)) (Romatoski and Hu, 2017), the temperature dependent trend provided as Equation (21) and (22) respectively. All supercells were first equilibrated in NVT ensemble for at least 50 ps and then continued to run 100 ps by using reverse non-equilibrium MD (rNEMD) method (Bordat and Muller-Plathe, 2002) to obtain the calculated viscosity.

$$\rho_{FLiNaK} = 2.53 - 0.00073T[C]\left[\frac{g}{cm^3}\right] \tag{21}$$

$$\rho_{NaF-ZrF_4} = 3.71 - 0.00089T[C]\left[\frac{g}{cm^3}\right] \tag{22}$$

During the rNEMD, an artificial velocity gradient is generated between the bottom and middle (along the z direction) in the simulation box representing shear. Based on the movement the exchanged momentum can be defined as the momentum difference along the x-direction between the bottom and middle (23).

$$P_{exchanged} = P_{x,\ bottom} - P_{x,\ middle} \tag{23}$$

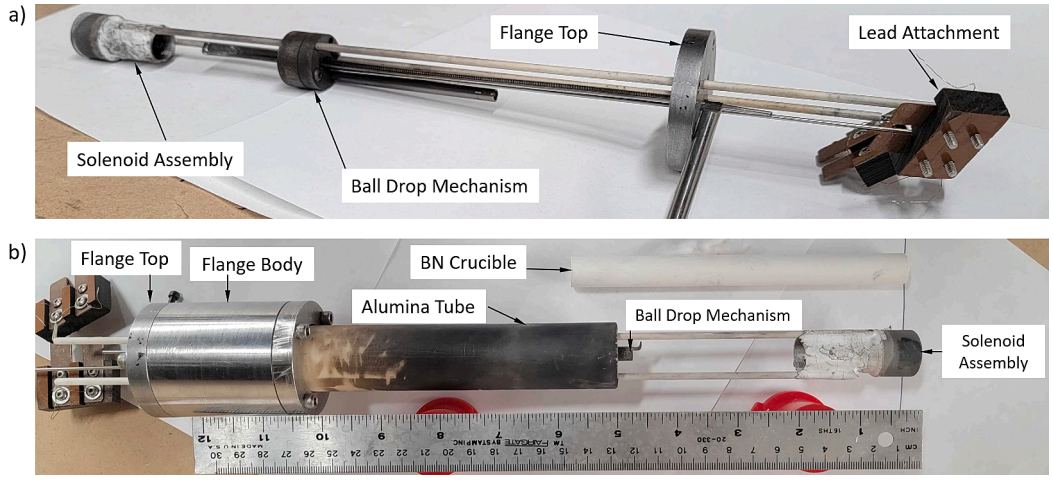

Fig. 8. a) fully assembled ball drop mechanism with coil assembly along and b) how it looks assembled with the alumina tube and flange body prior to inserting the bn crucible into the coils placing the assembly into the furnace.

This momentum flux is proportional to the product of the viscosity and velocity gradient, where t is time, S_{xy} is the area of the x-y plane of the simulation box, v_x is the partial velocity along the x direction, and η is the viscosity (24).

$$\frac{\sum P_{exchanged}}{2tS_{xy}} = \eta \frac{\partial v_x}{\partial z} \tag{24}$$

3. Results

Experimental measurements are compared to former studies of the same or similar composition in the case of NaF-ZrF_4. Viscosity was evaluated based on the same density trends as used in the MD simulations (21, 22). Experimental and MD data sets for each material is fit to the Arrhenius equation (25) for comparison. Results for FLiNaK, shown in Fig. 9, show good agreement with literature data, but do not match any one study. Trends are extrapolated beyond experimental data ranges for comparison with rNEMD data. Table 1 shows the Arrhenius coefficients (24) including additional ones not plotted in Fig. 9.

$$\mu[Pa \bullet s] = Aexp(E/T[K]) \tag{25}$$

Similarly, results for $NaFZrF_4$ are plotted in Fig. 10 with the relevant Arrhenius coefficients shown in Table 2. Similar compositions are shown in this case because of the limited information of the selected composition (53–47 mol%).

Standard error of mean is calculated with 95 % confidence. Temperature variation, ball diameter tolerance and signal variation are the most impactful sources of error. The highest error occurs at the lowest temperature for both salts. Other factors not considered but likely minimal effect include sensor spacing, natural convection and the accuracy of reported density values. End effects are also not accounted for.

The resultant Arrhenius trends from MD modeling shows good agreement to former studies where increasing temperature shows decreasing error. For both MD and experimental data, as the temperature approaches the melting point, error increases. Additionally, for FLiNaK, MD results deviate from experimental data at low temperatures. In contrast NaF-ZrF_4 deviates at high temperatures. Percent difference between MD and experimental data for both salts is presented in Table 3 for select temperatures based on the given Arrhenius trends.

4. Discussion & conclusion

This study demonstrates the applicability of a falling ball viscometer for making rapid measurements in high temperature molten salts. An accurate relationship can be established for this system between velocity and viscosity at Reynold's Number up to Re = 300 using numerical modeling methods. Additionally, there is good agreement with some

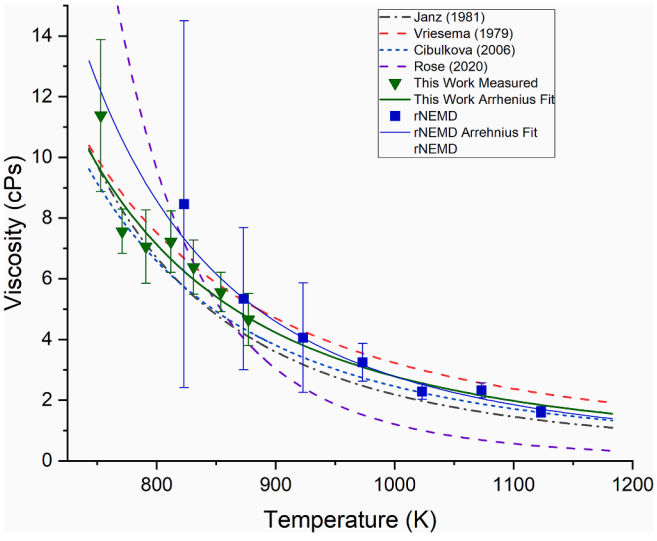

Fig. 9. As measured FLiNaK viscosity as a function of temperature with an exponential-Arrhenius fit compared to selected former studies.

Table 1
Viscosity $[Pa \bullet s]$ FLiNaK Eutectic Arrhenius Coefficients (Equation (8).

Study	A	E	Reported Uncertainty
Janz (1981) (Sohal et al., 2002)	2.48E-2	4478.62	2 %
Vriesema (1979) (Sohal et al., 2002; Vriesema, 1979)	1.1E-1	3379	–
Cibulkova (2006) (Cibulková et al., 2006)	4.74E-2	3947	2.5 %
Ambrosek (2009) (Ambrosek et al., 2009)	4E-2	4170	–
Kubíková (2012) (Kubikova et al., 2012)	3.80E-2	4565	0.7E-2 $[Pa \bullet s]$ (SD)*
Rose (2020) (Rose et al., 2022)	3E-2	8300	30–50 % (Estimated from graphic)
MD (This Work)	3.11E-2	4495.75	10–70 %
This Work	6.48E-2	3761.6	5–10 %

*Uncertainty reported as standard deviation.

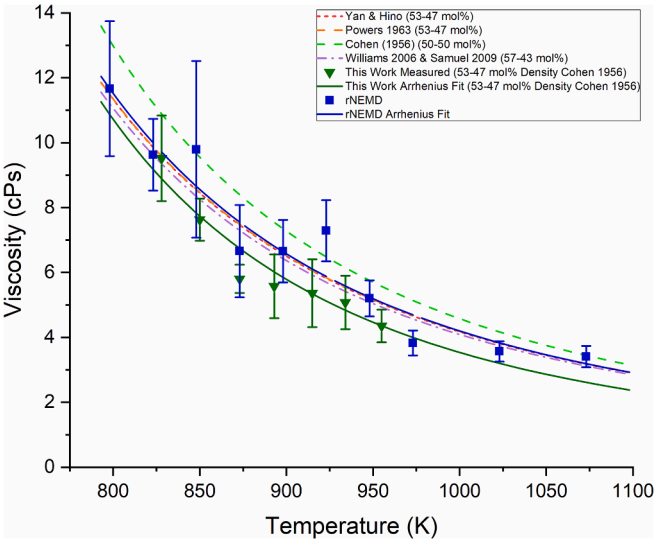

Fig. 10. As measured NaF-ZrF_4 (53–47 mol%) viscosity as a function of temperature with an exponential-Arrhenius fit compared to selected former studies.

Table 2
NaF-ZrF_4 (53–47 mol%) and similar compositions Viscosity $[Pa \bullet s]$ Arrhenius Coefficients (Equation (8).

Source	A	E	Reported Uncertainty
Powers (1963) (53–47 mol%) (Romatoski and Hu, 2017)	7.8E-2	3984	10 %-20 %
Cohen (1956) (50–50 mol%) (Romatoski and Hu, 2017; Cohen and Jones, 1957)	7.09E-2	4168	10 %
Williams (2006) (57–43 mol%) (Romatoski and Hu, 2017)	7.67E-2	3977	–
Yan & Hino (2011) (53–47 mol%) (Romatoski and Hu, 2017)	7.667E-2	3997	10 %
MD (This Work)	7.427E-2	4035.179	6–27 %
This Work	4.202E-2	4433.4	3–8.5 %

Table 3
Percent Difference between MD and Experimental Results of Select Temperatures.

Temperature (K)	FLiNaK Percent Difference	NaF-ZrF_4 Percent Difference
825	16.93	9.08
875	11.14	12.13
925	6.22	14.92
975	1.99	17.49

variation between experimental results, MD results, and previously reported literature values.

The variation in and between experimental results, MD results and other sources could be caused by many possible factors. Errors from experimental results could include non-optimal circuitry that causes variability in determining ball location due to noise from the Arduino power supply and the sampling method selected. Another cause could be related to volatility or reactivity that increases as temperature increases, more easily identified in NaF-ZrF_4. This salt is known to have increased volatility leading to loss of ZrF_4 at temperatures above 973 K (Sohal et al., 2002). Additionally, these salts are susceptible to impurities from corrosion products, trace oxygen and trace moisture in the environment (Misra and Whittenberger, 1987). This effect of oxygen and moisture could not be completely removed from the glove box or from precursor materials, and results in the formation of oxyfluoride and oxide (Figure S-2) (Holcomb and Cetiner, 2010). In these salts, impurities are more likely to target the larger cations (K and Zr respectively). Experimental samples are expected to end up with a loss of large cation-fluorine bonds, effecting the viscosity results (Chan et al., 2023; Galashev et al., 2023). While our samples do not show significant change in composition by EDS and ICP analysis, excessive variation in composition could cause enough deviation to see a difference from the ideal compositional represented in rNEMD simulations or experiments with higher environmental control.

It is also important to note that these values are highly dependent on the density values used for analysis. It is important to take this into consideration, both under the context of the MD and experimental results, especially for cases when ρ_{fluid} and ρ_{sphere} are more similar, as is the case with NaF-ZrF_4. Because the percentage change of the difference is higher, this results in larger variations in analyzed viscosity in these cases, which could additionally explain the deviation of experimental values from literature values. It is recommended that density is measured in parallel to using this method (or any other density dependent method, such as the rolling ball viscometer or oscillatory viscometer) where samples are prepared and tested under the same procedural guidelines and conditions for the best results. (Korklep and Oye, 1979; Ito et al., 1989; Birri et al., 2023; Levy, 2024).

The general factors affecting the MD results are simulation time and supercell size (number of total atoms in systems), short time and small cells may not be able to represent the properties of bulk material sufficiently. Another possible factor is the accuracy of PFP potentials in Matlantis; even though the potentials are trained directly from DFT, some accuracy and description must be sacrificed to improve the calculation speed. As for the larger error bar at relatively low temperatures especially around the melting point of the salts, low temperatures may cause some ions' kinetic energy to be very close or even lower to the diffusion barrier, thus these ions will have low self-diffusivities compared to others and resulting large discrepancy of diffusivities of overall same type ions; finally, this difference will also be reflected in the viscosity results.

Future work with results from studies of x-ray measurement techniques of similarly prepared samples and MD simulations intends to explore these relationships between liquid atomic structure and thermophysical properties further (Wadehra et al., 2024; Guo et al., 2023).

Similarly, sphere and crucible material may need to be reconsidered especially if working with alternative molten salts. Titanium was selected for this study based on its high melting point and low density to minimize the difference between ρ_{fluid} and ρ_{sphere} so that terminal velocity is achieved in a shorter distance and Re is minimized. Ti is known to not have good corrosion resistance with fluoride salts, particularly FLiNaK (Patel et al., 2023). For this method, due to the quick sampling rates, the duration of salt exposure to Ti in this experiment is limited (several hours if changing between several temperatures) and is likely to have minimal effect. Post-measurement characterization of the salts shows no measurable amount of Ti in either salt, but trace amounts could still be present.

If the ball material is changed, it is believed that the system can be scaled accordingly to accommodate denser spheres that may otherwise take longer to reach terminal velocity. The extent of this would need to be determined. The measurements in this work only test $Re < 300$ and a $r_{sphere}/R_{crucible}$ ratio of up to 33 %. In these cases, sphere and crucible diameter can be modified, but a more sensitive detection method would be required for smaller diameter spheres. Even with this consideration, there is a limit to the range achievable. As Re increases the viscous component of the drag becomes negligible. Also, the dynamics change in the vicinity between the ball and crucible wall as the $r_{sphere}/R_{crucible}$ ratio increases.

In conclusion, this work has demonstrated the ability for a falling ball viscometer to be applied to a high temperature application for fast, reasonably reliable measurements, but requires additional considerations to improve accuracy and applicability.

CRediT authorship contribution statement

Alexander Levy: Writing – original draft, Visualization, Software, Resources, Methodology, Investigation, Formal analysis, Data curation. **Yifan Zhang:** Writing – original draft, Visualization, Software, Resources, Methodology, Investigation, Formal analysis. **Haoxuan Yan:** Writing – review & editing, Visualization, Validation, Resources, Methodology. **Anubhav Wadehra:** Writing – review & editing, Visualization, Validation, Resources, Investigation. **Yu Zhong:** Writing – review & editing, Supervision, Project administration, Funding acquisition, Conceptualization. **Karl Ludwig:** Writing – review & editing, Supervision, Project administration, Funding acquisition, Conceptualization. **Uday Pal:** Writing – review & editing, Supervision, Project administration, Funding acquisition, Conceptualization.

Declaration of competing interest

The authors declare that they have no known competing financial interests or personal relationships that could have appeared to influence the work reported in this paper.

Data availability

Data will be made available on request.

Acknowledgements

This research at Boston University and the Worcester Polytechnic Institute was supported by the US Department of Energy (DOE) NEUP program [Grant Number 20-19373], and the US National Science Foundation (NSF) [Award No. CMMI-1937818 and CMMI 1937829].

Appendix A. Supplementary data

Supplementary data to this article can be found online at https://doi.org/10.1016/j.nucengdes.2024.113612.

References

Ambrosek, J., Anderson, M., Sridharan, K., Allen, T., 2009. Current Status of Knowledge of Fluoride Salt (FLiNaK) Heat Transfer. Thermal Hydraulics. 165, 166–173. https://doi.org/10.13182/NT165-166.

Bhatnagar, P., Siddiqui, S., Sreedhar, I., Parameshwaran, R., 2022. Molten Salts: Potential candidates for thermal energy storage applications. Energy Research 46, 17755–17785. https://doi.org/10.1002/er.8441.

Bhattad, A., 2023. Review on viscocity measurement: devices, methods and models. Journal of Thermal Analysis and Calorimetry 148, 6527–6543. https://doi.org/10.1007/s10973-023-12214-0.

Birri, A., Termini, N., Rose, P.J., Chapel, S., Andrews, H., Ezell, N.D.B., 2023. Developement and demonstration of a rolling ball viscometer for molten salts with near-minimum liquidus NaCl-KCl. Thermal Science and Engineering Progress 44, 102029. https://doi.org/10.1016/j.tsep.2023.102029.

Bordat, P., Muller-Plathe, F., 2002. The shear viscosity of molecular fluids: A calculation by reverse nonequilibrium molecular dynamics. The Jounral of Chemical Physics 116, 3360–3362. https://doi.org/10.1063/1.1436124.

Bougas, A., Stamatoudis, M., 1993. Wall Factor for Acceleration and Terminal Velocity of Falling Spheres at HIgh Reynolds Numbers. Chemical Engineering Technology 16, 314–317. https://doi.org/10.1002/ceat.270160506.

Brizard, M., Megharfi, M., Verdier, C., Mahe, E., 2005. Design of a High Precision Falling Ball Viscometer. Review of Scientific Instruments 76 (025109), 2005. https://doi.org/10.1063/1.1851471.

Chan, H.L., Romanovskaia, E., Romanovski, V., Sur, D., Hong, M., Hosemann, P., Scully, J.R., 2023. Corrosion Electrochemistry of Chromium in Molten FLiNaK Salt at 600 °C. Journal of the Electrochemical Society. 170, 081502. https://doi.org/10.1149/1945-7111/ace8c0.

Cibulková, J., Cibulková, M., Vasiljev, R., Kremenetsky, V., Boča, M., 2006. Density and Viscosity of the (LiF+NaF+KF)eut(1)+K2TaF7(2)+Ta2O5 (3) Melts. Journal of Chemical Engineering 51, 984–987. https://doi.org/10.1021/je050490g.

Cohen, S.I., Jones, T.N., 1957. Viscocity Measurements On Molten Fluoride Mixtures. Oak Ridge National Labratory. https://doi.org/10.2172/4803933.

COMSOL, 2024. Terminal Falling Velocity of a Sand Grain (Application ID 983) COMSOL Application Gallery. https://www.comsol.com/model/terminal-falling-velocity-of-a-sand-grain-983.

Cottrell, W.B. Hungerford, H. E., Leslie, J. K., Meem, J. L., 1955. Operation of the Aircraft Reactor Experiment., Oaktridge National Lab, Oakridge TN, 1955. ORNL-1845. DOI: 10.2172/4237975.

Feng, S., Graham, A.L., Reardon, P.T., Abbott, J., Mody, L., 2006. Improving Falling Ball Tests for Viscosity Determination. Journal of FLuids Engineering 128, 157–163. https://doi.org/10.1115/1.2137345.

G.E.N.-IV International-Forum, 2009. GIF R&D Outlook for Generation IV Nuclear Energy Systems.

Galashev, A.Y., Rakhmanova, O.R., Abramova, K.A., Katin, K.P., Maslov, M.M., Tkacheva, O.Y., Rudenko, A.V., Kataev, A.A., Zaikov, Y.P., 2023. Molecular Dynamics and Experimental Study of the Effect of CeF3 and NDF3 additives on Pyshical properties of FLiNaK. The Jounral of Phsycal Chemistry B 127, 1197–1208. https://doi.org/10.1021/acs.jpcb.2c06915.

Guo, J., Zhang, Y., Ludwig, K., Yan, H., Levy, A., Wadehra, A., Gao, M.C., Chris, B., Rose, M., Condon, N., Powell, A., Zhong, Y., Pal, U., 2023. X-ray and molecular dynamics study of the temperature-dependent structure of FLiNaK. Nuclear Materials and Engineering 37, 101530. https://doi.org/10.1016/j.nme.2023.101530.

Happel, J., Brenner, H., Low Reynolds number hydrodynamics, 1993. Boston: Martinus Njhoff Publishers, First paperback edition, The Hague.

Holcomb, D. E., Cetiner, S. M., 2010. An Overview of Liquid-Fluoride-Salt Heat Transport Systems, Oakridge National Lab, Oak Ridge TN. ORNL/TM-2010/156.

Ito, T., Kojima, N., Nagashima, 1989. Redetermination of the Viscocity of Molten NaCl at Elevated Temperatures. Interhantional Journal of Thermophsics. 10, 819–831. https://doi.org/10.1007/BF00514478.

Johnson, T.A., Patel, V.C., 1999. Flow pas a sphere up to a reynolds number of 300. Journal of Fluid Mechanics 378, 19–70. https://doi.org/10.1017/S0022112098003206.

Kobbekaduwa, K., Wijayaratnam W. 2012. Data Acquisition System for a Falling-Sphere Viscometer. Proceedings of the 28th Technical Sessions, 28, 45-53. 10.13140/RG.2.1.1930.5685.

Korklep, K., Oye, K.A., 1979. An absolute oscillating-cylinder (or cup) viscometer for high temperatures. Great Britain: Journal of Physical Engineering: Science Instrumentation 12, 875–885. https://doi.org/10.1088/0022-3735/12/9/021.

Kubikova, B., Viliam, P., Macková, I., Boca, M., 2012. Surface tension and viscosity of the molten (LiF–NaF–KF)eut–K2ZrF6 system. Monatshefte Für Chemie 143, 1459–1462. https://doi.org/10.1007/s00706-012-0832-3.

Levy, A. 2024, High Measurement Rate Property Measurement Methods for Molten Salts, [Doctoral dissertation, Boston University]. Boston University Institutional Repository.

Liu, H., Zhang, X., He, S., He, D., Shang, Y., Yu, H., 2022. Molten salts for recharable batteries. Materials Today 60, 128–157. https://doi.org/10.1016/j.mattod.2022.09.005.

Lyu, P, 2015. How Do I Compute Lift and Drag?. https://www.comsol.com/blogs/how-do-i-compute-lift-and-drag/. (accessed 29 April 2024).

Mao, Y., Hu, Y.-H., Hu, X.-Y., Yao, L.-Q., Li, H., Lin, L.-M., Tang, P., Li, H., Chen, S., Li, J.-M., Chen, G.-L., 2022. Molten Salts assisted Interfacial Engineering for Efficient and Low-Cost Full-inorganic Antimony Sulfide Solar Cells. Advanced Functional Materials 32, 2208409. https://doi.org/10.1002/adfm.202208409.

Martinez, L., et al., 2009. PACKMOL: A package for building initial configurations of molecular dynamics simulations. Jounral of Computational Chemistry 30, 2157–2164. https://doi.org/10.1002/jcc.21224.

Misra, A. K., Whittenberger, J. D., 1987. Fluoride Salts and Container Materials for Thermal Energy Storage Appllications in Temperature Range 973 to 1400K. Lewis Research Center, NASA, Cleveland Ohio.19870014593.

Patel, K., Mahajan, C., Muskerri, S. Mukherjee, S., 2023. Corrosion Behavior of Refractory High-Entropy Alloys in FLiNaK Molten Salts/ Metals, 13. DOI: 10.3390/met13030450.

Powell, L.R., Mondy, L.A., Stoker, G.G., Milliken, J.W., Graham, L.A., 1989. Development of a falling ball rheometer with applications to opaque systems: measurements of the rheology of suspensions of rods. Journal of Tehology 33, 1173–1188. https://doi.org/10.1122/1.550054.

Romatoski, R., Hu, L., 2017. Fluoride salt coolant properties for nuclear reactor applications: A review. Annals of Nuclear Energy 109, 635–647. https://doi.org/10.1016/j.anucene.2017.05.036.

Rose, M.A., Wu, E., Williamson, M.A., 2022. Thermophysical Property Measurements: Improved Density, Viscosity and Thermal Diffusivity Methods. Argonne National Lab. ANL/CFCT-20/38.

Serrano-Lopez, R., Cuesta-Lopez, F.S., 2013. Molten Salts databases for energy applications. Chemical Engineering and Processing: Proess Intensification 73, 87–102. https://doi.org/10.1016/j.cep.2013.07.008.

Singh, A.V., Sharma, L., Gupta-Bhaya, P., 2012. Studies on Falling Ball Viscometry. Arxiv. https://doi.org/10.48550/arXiv.1202.1400.

Sobczak, R., 1986. Viscosity measurement by spheres falling in a magnetic field. Rheologica Acta 25, 175–179. https://doi.org/10.1007/BF01332136.

Sohal, M.S., Ebner, M.A., Sabharwall, P., Sharpe, P., 2002. Engineering Database of Liquid Salt Thermophysical and Thermochemical Properties. Idaho National Labratory. https://doi.org/10.2172/980801.

Takamoto, S., Shinagawa, C., Motoki, D., et al., 2022. Towards universal nural network potential for material discover applicable to arbitrary combination of 45 elements. Nature Communications 13, 2991. https://doi.org/10.1038/s41467-022-30687-9.

Tkacheva, O.Y., Rudenko, A.V., Kataev, A.A., Mushnikov, P.N., Kxholkinam, A.S., Zaikov, Y.P., 2022. The Viscocity of Molten Salts based on the LiF-BeF2 System. Metallurgy of Nonferrous Metals 63, 276–283. https://doi.org/10.3103/S1067821222030117.

Vriesema, B., et al., 1979. Aspects of molten fluorides as heat transfer agents for power generation. Delft University of Technology.

Wadehra, A., Chahal, R., Banerjee, S., Levy, A., Zhang, Y., Yan, H., Olds, D., Zhong, Y., Pal, U., Lam, S., Karl, K., 2024. X-ray and molecular dynamics study of the temperature-dependent structure of molten NaF-ZrF4. Arxiv. https://doi.org/10.48550/arXiv.2403.06049.

Wahl, H.v., Richter, T., Frie, S., Hagemeier, T., 2021. Falling balls in a viscous fluid with contact: Comparing numerical simulations with experimental data. Physics of Fluids 33, 033304. https://doi.org/10.1063/5.0037971.

Williams, D.F., Toth, L.M., Clarno, K.T., 2006. Assessment of Candidate Molten Salt Coolants for the Advanced High-Temperature Reactor (AHTR). Oakridge National Lab. Oak Ridge TN. ORNL/TM-2006/12.

Molten Salt Chemistry Workshop. 2017. Report for the US Department of Energy, Office of Nuclear Energy Workshop, Oakridge National Lab, Oak Ridge TN.